

# COMPRESSIVE INVERSE SCATTERING II. SISO MEASUREMENTS WITH BORN SCATTERERS

ALBERT C. FANNJIANG

**ABSTRACT.** Inverse scattering methods capable of compressive imaging are proposed and analyzed. The methods employ randomly and repeatedly (multiple-shot) the single-input-single-output (SISO) measurements in which the frequency, the chosen incidence and the sampling angle are related in a precise way and are capable of recovering exactly (point of extended) scatterers of sufficiently low sparsity.

For point targets, various sampling techniques are proposed to transform the scattering matrix into the random Fourier matrix. Two schemes are particularly interesting: The first one employs multiple frequencies with the sampling angle always in the back-scattering direction resembling the synthetic aperture (SA) imaging; the second employs only single frequency with the sampling angle in the (nearly) forward scattering direction in the high frequency limit, resembling that of the X-ray tomography.

For extended targets, the Littlewood-Paley basis is used in analysis. A specially designed sampling scheme then transforms the scattering matrix into a block-diagonal matrix with each block being the random Fourier matrix corresponding to one of the multiple dyadic scales of the extended target. In other words by the Littlewood-Paley basis and the proposed sampling scheme the different dyadic scales of the target are decoupled and therefore can be reconstructed scale-by-scale by the proposed method.

## 1. INTRODUCTION

Consider the scattering of the incident plane wave

$$(1) \quad u^i(\mathbf{r}) = e^{i\omega \mathbf{r} \cdot \mathbf{d}}$$

by the variable refractive index  $n^2(\mathbf{r}) = 1 + \nu(\mathbf{r})$  where  $\mathbf{d}$  is the incident direction. The scattered field satisfies the Lippmann-Schwinger equation [9]

$$(2) \quad u^s(\mathbf{r}) = \omega^2 \int \nu(\mathbf{r}') (u^i(\mathbf{r}') + u^s(\mathbf{r}')) G(\mathbf{r}, \mathbf{r}', \omega) d\mathbf{r}', \quad \mathbf{r} \in \mathbb{R}^d, \quad d = 2, 3$$

where  $G(\mathbf{r}, \mathbf{r}', \omega)$  is the Green function of the operator  $-(\Delta + \omega^2)$ . We assume that the wave speed is unity and hence the frequency equals the wavenumber  $\omega$ .

The scattered field has the far-field asymptotic

$$(3) \quad u^s(\mathbf{r}) = \frac{e^{i\omega|\mathbf{r}|}}{|\mathbf{r}|^{(d-1)/2}} (A(\hat{\mathbf{r}}, \mathbf{d}, \omega) + \mathcal{O}(|\mathbf{r}|^{-1})), \quad \hat{\mathbf{r}} = \mathbf{r}/|\mathbf{r}|,$$

where  $A$  is the scattering amplitude. In inverse scattering theory, the scattering amplitude is the measurement data determined by the formula [9]

$$(4) \quad A(\hat{\mathbf{r}}, \mathbf{d}, \omega) = \frac{\omega^2}{4\pi} \int d\mathbf{r}' \nu(\mathbf{r}') u(\mathbf{r}') e^{-i\omega \mathbf{r}' \cdot \hat{\mathbf{r}}}$$

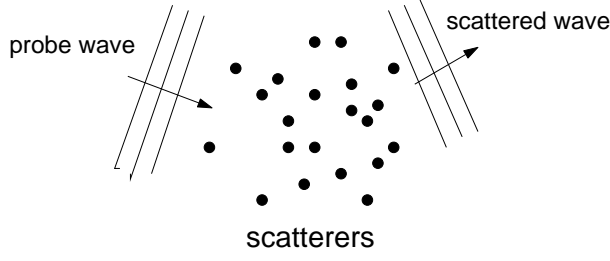


FIGURE 1. Far-field imaging of discrete scatterers

The main objective of inverse scattering then is to reconstruct the medium inhomogeneities  $\nu$  from the knowledge of the scattering amplitude. In Part I [13] and the present paper we study the inverse scattering problem using the compressed sensing techniques. In [13] we analyze the imaging method with the single-input-multiple-output (SIMO) measurements in which for every incident plane wave the scattering amplitude is measured at multiple sampling directions. In this paper we focus on the methods with the single-input-single-output (SISO) measurements in which for every incident plane wave the scattering amplitude is measured at only one sampling direction.

In Sections 2, we discuss the case of point scatterers and propose several sampling schemes to transform the scattering matrix into the random Fourier matrix which is amenable to the compressed sensing techniques. One scheme employs multiple frequencies with the sampling angle always in the back-scattering direction resembling the synthetic aperture (SA) imaging; another scheme employs only single frequency with the sampling angle in the (nearly) forward scattering direction in the high frequency limit, resembling that of the X-ray tomography. We numerically test these sampling methods and compare their success probabilities in Section 3. In Section 4 we analyze extended targets using the Littlewood-Paley basis and propose a sampling scheme to block-diagonalize the scattering matrix. Each block is in the form of random Fourier matrix and corresponds to one dyadic scale of the target. Hence our method has the capability of imaging the target scale-by-scale by the compressed sensing techniques. We conclude and comment on the issue of resolution in Section 5.

## 2. POINT SCATTERERS

For the simplicity of notation, we will focus on two dimensions below.

We consider the medium with point scatterers located in a square lattice  $\mathcal{M} = \{\mathbf{x}_i = (x_i, z_i) : i = 1, \dots, m\}$  of spacing  $\ell$ . The total number  $m$  of grid points in  $\mathcal{M}$  is a perfect square. Without loss of generality, assume  $x_j = j_1\ell, z_j = j_2\ell$  where  $j = (j_1 - 1)\sqrt{m} + j_2$  and  $j_1, j_2 = 1, \dots, \sqrt{m}$ . Let  $\nu_j, j = 1, \dots, m$  be the strength of the scatterers. Let  $\mathcal{S} = \{\mathbf{x}_{i_j} = (x_{i_j}, z_{i_j}) : j = 1, \dots, s\}$  be the locations of the scatterers. Hence  $\nu_j = 0, \forall \mathbf{r}_j \notin \mathcal{S}$ .

For the discrete medium the scattering amplitude becomes a finite sum

$$(5) \quad A(\hat{\mathbf{r}}, \mathbf{d}, \omega) = \frac{\omega^2}{4\pi} \sum_{j=1}^m \nu_j u(\mathbf{x}_j) e^{-i\omega \mathbf{x}_j \cdot \hat{\mathbf{r}}}.$$

Unlike [13] which covers both linear and nonlinear scattering, here we work exclusively under the Born approximation in which the exciting field  $u(\mathbf{x}_j)$  is replaced by the incident field  $u^i(\mathbf{x}_j)$ ; unlike [13] which deals exclusively with one frequency, here we will work with multiple frequencies.

Let  $\mathbf{d}_l, \hat{\mathbf{r}}_l, l = 1, \dots, n$  be various incident and sampling directions to be determined later. Define the measurement vector  $Y = (Y_l) \in \mathbb{C}^n$  with

$$(6) \quad Y_l = \frac{4\pi}{\omega^2} A(\hat{\mathbf{r}}_l, \mathbf{d}_l, \omega_l), \quad l = 1, \dots, n.$$

The measurement vector is related to the target vector  $X = (\nu_j) \in \mathbb{C}^m$  by the sensing matrix  $\mathbf{A}$  as  $Y = \mathbf{A}X$ . Let  $\theta_l, \tilde{\theta}_l$  be the polar angles of  $\mathbf{d}_l, \hat{\mathbf{r}}_l$ , respectively. The  $(l, j)$ -entry of  $\mathbf{A} \in \mathbb{C}^{n \times m}$  is

$$(7) \quad e^{-i\omega_l(z_j \sin \tilde{\theta}_l + x_j \cos \tilde{\theta}_l)} u^i(\mathbf{x}_j) = e^{i\omega_l \ell(j_2(\sin \theta_l - \sin \tilde{\theta}_l) + j_1(\cos \theta_l - \cos \tilde{\theta}_l))}, \quad j = (j_1 - 1) + j_2.$$

As in [13] we reconstruct  $X$  as the solution of the  $L^1$ -minimization, called Basis Pursuit (BP):

$$(8) \quad \min \|X\|_1 \quad \text{s.t.} \quad \mathbf{A}X = Y$$

which can be solved by linear programming or by various greedy algorithms [2, 8, 10, 12].

A fundamental notion in compressed sensing under which BP yields the unique exact solution is the restrictive isometry property (RIP) due to Candès and Tao [6]. Precisely, let the sparsity  $s$  of a vector  $Z \in \mathbb{C}^m$  be the number of nonzero components of  $Z$  and define the restricted isometry constant  $\delta_s$  to be the smallest positive number such that the inequality

$$(1 - \delta_s) \|Z\|_2^2 \leq \|\mathbf{A}Z\|_2^2 \leq (1 + \delta_s) \|Z\|_2^2$$

holds for all  $Z \in \mathbb{C}^m$  of sparsity at most  $s$ . For the target vector  $X$  let  $X_s$  denote the best  $s$ -sparse approximation of  $X$  in the sense of  $L^1$ -norm, i.e.

$$X^{(s)} = \operatorname{argmin} \|Z - X\|_1, \quad \text{s.t.} \quad \|Z\|_0 \leq s$$

where  $\|Z\|_0$  denotes the number of nonzero components, called the sparsity, of  $Z$ . Clearly,  $X^{(s)}$  consists of the  $s$  largest components of  $X$ .

Now we state the fundamental result of the RIP approach [3] which is an improvement of the results of [4, 6].

**Proposition 1.** [3] *Suppose the restricted isometry constant of  $\mathbf{A}$  satisfies the inequality*

$$(9) \quad \delta_{2s} < \sqrt{2} - 1$$

*Then the solution  $\hat{X}$  by BP (8) satisfies*

$$(10) \quad \|\hat{X} - X\|_1 \leq C_0 \|X - X^{(s)}\|_1$$

$$(11) \quad \|\hat{X} - X\|_2 \leq C_0 s^{-1/2} \|X - X^{(s)}\|_1$$

*for some constant  $C_0$ . In particular, if  $X$  is  $s$ -sparse, then the recovery is exact.*

We wish to write the  $(l, j)$ -entry of the sensing matrix in the form

$$(12) \quad e^{i\pi(j_1 \xi_l + j_2 \zeta_l)}, \quad j = (j_1 - 1)\sqrt{m} + j_2, \quad j_1, j_2 = 1, \dots, \sqrt{m}, \quad l = 1, \dots, n$$

where  $\xi_l, \zeta_l$  are independently and uniformly distributed in  $[-1, 1]$  in view of the following theorem.

**Proposition 2.** [16] *Suppose*

$$(13) \quad \frac{n}{\ln n} \geq C\delta^{-2}\sigma \ln^2 \sigma \ln m \ln \frac{1}{\alpha}, \quad \alpha \in (0, 1)$$

for a given sparsity  $\sigma$  where  $C$  is an absolute constant. Then the restricted isometry constant of the matrix with entry (12) satisfies

$$\delta_\sigma \leq \delta$$

with probability at least  $1 - \alpha$ .

See [4, 7, 17] for the case when  $\xi_l, \zeta_l$  belong to the discrete subset of  $[-1, 1]$  of equal spacing  $2/\sqrt{m}$ .

To construct a sensing matrix of the form (12) we proceed as follows. Write  $(\xi_l, \zeta_l)$  in the polar coordinates

$$(\xi_l, \zeta_l) = \rho_l(\cos \phi_l, \sin \phi_l), \quad \rho_l = \sqrt{\xi_l^2 + \zeta_l^2} \leq \sqrt{2}$$

and set

$$\begin{aligned} \omega_l(\cos \theta_l - \cos \tilde{\theta}_l) &= \sqrt{2}\rho_l\Omega \cos \phi_l \\ \omega_l(\sin \theta_l - \sin \tilde{\theta}_l) &= \sqrt{2}\rho_l\Omega \sin \phi_l \end{aligned}$$

where  $\Omega$  is a parameter to be determined later (27). Equivalently we have

$$(14) \quad -\sqrt{2}\omega_l \sin \frac{\theta_l - \tilde{\theta}_l}{2} \sin \frac{\theta_l + \tilde{\theta}_l}{2} = \Omega\rho_l \cos \phi_l$$

$$(15) \quad \sqrt{2}\omega_l \sin \frac{\theta_l - \tilde{\theta}_l}{2} \cos \frac{\theta_l + \tilde{\theta}_l}{2} = \Omega\rho_l \sin \phi_l.$$

This set of equations determines the single-input- $(\theta_l, \omega_l)$ -single-output- $\tilde{\theta}_l$  mode of sampling.

The following implementation of (14)-(15) is natural. Let the sampling angle  $\tilde{\theta}_l$  be related to the incidence angle  $\theta_l$  via

$$(16) \quad \theta_l + \tilde{\theta}_l = 2\phi_l + \pi,$$

and set the frequency  $\omega_l$  to be

$$(17) \quad \omega_l = \frac{\Omega\rho_l}{\sqrt{2} \sin \frac{\theta_l - \tilde{\theta}_l}{2}}.$$

Then the entries (7) of the sensing matrix  $\mathbf{A}$  have the form

$$(18) \quad e^{i\sqrt{2}\Omega\ell(j_1\xi_l+j_2\zeta_l)}, \quad l = 1, \dots, n, \quad j_1, j_2 = 1, \dots, \sqrt{m}.$$

By the square-symmetry of the problem, it is clear that the relation (16) can be generalized to

$$(19) \quad \theta_l + \tilde{\theta}_l = 2\phi_l + \eta\pi, \quad \eta \in \mathbb{Z},$$

Indeed, it will be seen below that any fixed  $\eta \in \mathbb{R}$  produces essentially the same result.

Let us focus on three specific measurement schemes.

**Scheme I.** The first case is that of  $\Omega$ -band limited signals, i.e.  $\omega_l \in [-\Omega, \Omega]$ . This and (17) lead to the constraint:

$$(20) \quad \left| \sin \frac{\theta_l - \tilde{\theta}_l}{2} \right| \geq \frac{\rho_l}{\sqrt{2}}.$$

The simplest way to satisfy (16) and (20) is to set

$$(21) \quad \phi_l = \tilde{\theta}_l = \theta_l + \pi,$$

$$(22) \quad \omega_l = \frac{\Omega \rho_l}{\sqrt{2}}$$

$l = 1, \dots, n$ . In this case the scattering amplitude is always sampled in the back-scattering direction. This resembles the synthetic aperture imaging which has been previously analyzed under the paraxial approximation in [15]. In contrast, the forward scattering direction with  $\tilde{\theta}_l = \theta_l$  almost surely violates the constraint (20).

**Scheme II.** The second case is that of single frequency no less than  $\Omega$ :

$$(23) \quad \omega_l = \gamma \Omega, \quad \gamma \geq 1, \quad l = 1, \dots, n.$$

To satisfy (19) and (17) we set

$$(24) \quad \theta_l = \phi_l + \frac{\eta \pi}{2} + \arcsin \frac{\rho_l}{\gamma \sqrt{2}}$$

$$(25) \quad \tilde{\theta}_l = \phi_l + \frac{\eta \pi}{2} - \arcsin \frac{\rho_l}{\gamma \sqrt{2}}$$

with  $\eta \in \mathbb{Z}$ . The difference between the incidence angle and the sampling angle is

$$(26) \quad \theta_l - \tilde{\theta}_l = 2 \arcsin \frac{\rho_l}{\gamma \sqrt{2}}$$

which diminishes as  $\gamma \rightarrow \infty$ . In other words, in the high frequency limit, the sampling angle approaches the incidence angle. This resembles the setting of the X-ray tomography.

**Scheme III.** The third case is that of unlimited frequency band. Let  $\theta_l$  be  $n$  arbitrary distinct numbers in  $[-\pi, \pi]$  and let  $\tilde{\theta}_l$  and  $\omega_l$  be determined by (19) and (17), respectively. The possibility of having a small divisor in (17) renders the bandwidth unlimited in principle.

The following result is an immediate consequence of Proposition 1 and Proposition 2.

**Theorem 1.** *Let  $\xi_l, \zeta_l$  be independently and uniformly distributed in  $[-1, 1]$  and let  $(\rho_l, \phi_l)$  be the polar coordinates of  $(\xi_l, \zeta_l)$ , i.e.*

$$(\xi_l, \zeta_l) = \rho_l (\cos \phi_l, \sin \phi_l).$$

*Let the probe frequencies  $\omega_l$ , the incidence angles  $\theta_l$  and the sampling angles  $\tilde{\theta}_l$  satisfy (16) and (17), for example, by Scheme I, II or III.*

*Suppose*

$$(27) \quad \Omega \ell = \pi / \sqrt{2}$$

*and suppose (13) holds with  $\sigma = 2s$  and any  $\delta < \sqrt{2} - 1$ . Then (9) is satisfied for the matrix  $\mathbf{A}$  with probability at least  $1 - \alpha$  and the bounds (10)-(11) hold true. In particular, every target vector of sparsity less than  $s$  can be exactly recovered by BP (8).*

Suppose the noise  $E$  is present in the measurement vector as described by

$$(28) \quad Y = \mathbf{A}X + E, \quad \|E\|_2 = \varepsilon > 0$$

and consider the relaxation scheme

$$(29) \quad \min \|Z\|_1, \quad \text{s.t.} \quad \|Y - \mathbf{A}Z\|_2 \leq \epsilon.$$

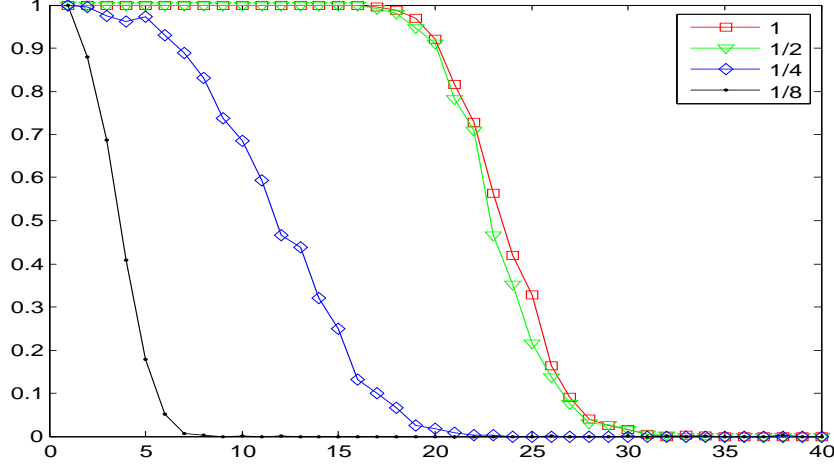


FIGURE 2. Success probabilities for Scheme I with (31). The label indicates the value of  $\eta$ .

The next result is a restatement of the result of [3] after applying Proposition 2 with  $\sigma = 2s, \delta < \sqrt{2} - 1$ .

**Theorem 2.** *Let  $Y$  be given by (28) and let  $\hat{X}$  be the solution to (29). Then under the assumptions of Theorem 1 we have*

$$(30) \quad \|\hat{X} - X\|_2 \leq C_0 s^{-1/2} \|X - X^{(s)}\|_1 + C_1 \varepsilon$$

with probability at least  $1 - \alpha$  where  $C_0$  and  $C_1$  are constants.

### 3. NUMERICAL RESULTS

Greedy algorithms have significantly lower computational complexity than linear programming and have provable performance under various conditions. For example under the condition  $\delta_{3s} < 0.06$  the Subspace Pursuit (SP) algorithm is guaranteed to exactly recover  $X$  via a finite number of iterations [10]. We have used SP for reconstruction in all our simulations with the following parameters:  $m = 2500, \ell = 1, \Omega = \pi/\sqrt{2}, n = 100$ . The probability of recovery is calculated by using 1000 independent runs.

To test Scheme I numerically, we use (22) and

$$(31) \quad \tilde{\theta}_l = \theta_l + \eta\pi, \quad \eta = 1, 1/2, 1/4, 1/8$$

to see if the deviations from (21) have any impact on performance. Their probabilities of recovery are plotted as a function of the sparsity in Figure 2. Clearly, the performance deteriorates rapidly as the difference between the sampling and incident angles decreases. In other words, the backward scattering direction is the optimal sampling direction.

Likewise, to test Scheme II numerically, we use (23),

$$(32) \quad \tilde{\theta}_l = \phi_l + \frac{\tilde{\eta}\pi}{2} - \arcsin \frac{\rho_l}{\gamma\sqrt{2}}, \quad \tilde{\eta} = 1, 1/2, 1/4,$$

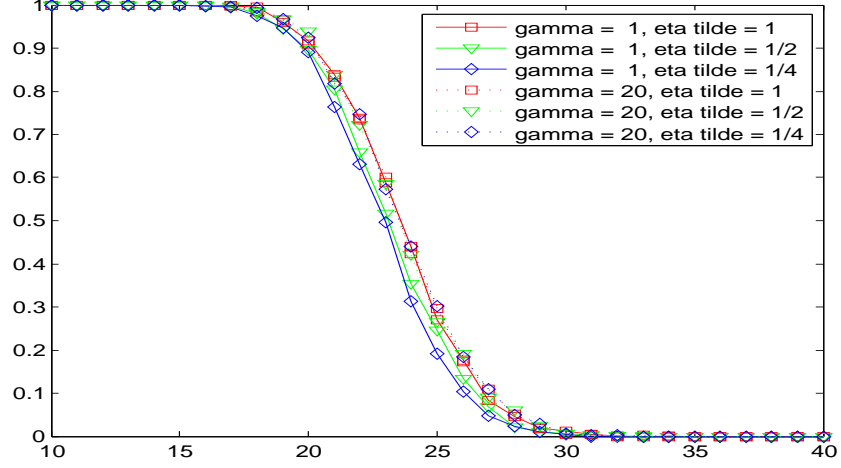


FIGURE 3. Success probabilities for Scheme II (a):  $\eta = 1, \tilde{\eta} = 1, 1/2, 1/4$  with  $\gamma = 1, 20$ .

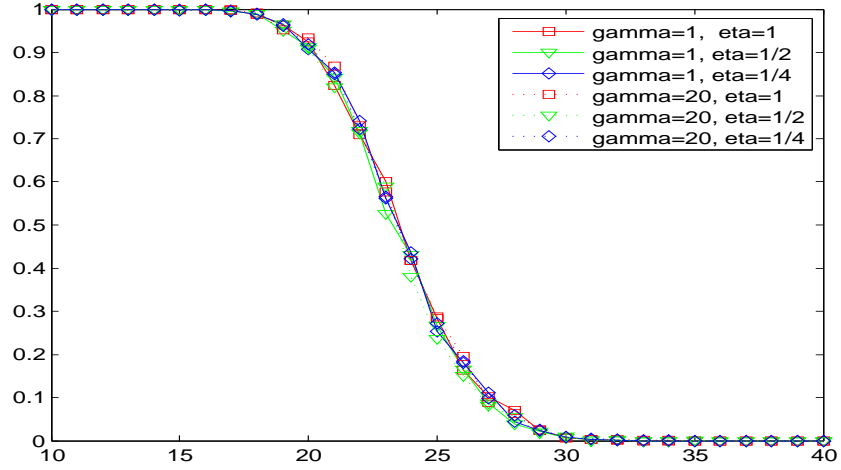


FIGURE 4. Success probabilities for Schemes II (b):  $\eta = \tilde{\eta} = 1, 1/2, 1/4$  with  $\gamma = 1, 20$ .

and (24) with (a)  $\eta = 1$  as well as (24) with (b)  $\eta = \tilde{\eta} = 1, 1/2, 1/4$ . Condition (26) is satisfied if and only if  $\eta = \tilde{\eta}$ .

The results for Case (a) at  $\gamma = 1, 20$  are shown in Figure 3 and the results for Case (b) with  $\eta = \tilde{\eta}$  at  $\gamma = 1, 20$  are displayed in Figure 4. The slight degradation in performance for e.g.,  $\eta = 1, \tilde{\eta} = 1/4, \gamma = 1$  results from the violation of (26) whose validity is important for  $\gamma$  close to unity. For sufficiently large  $r$ , say  $\gamma = 20$ , the violation of (26) does not affect the performance (see below). On the other hand, when (26) holds, the performance is essentially independent of both  $\gamma$  and  $\tilde{\eta}$ , Figure 4.

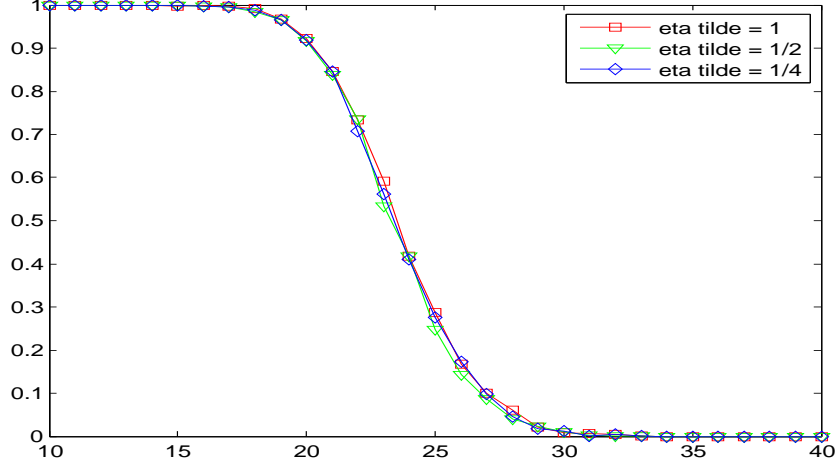


FIGURE 5. Success probabilities for Scheme III with (33).

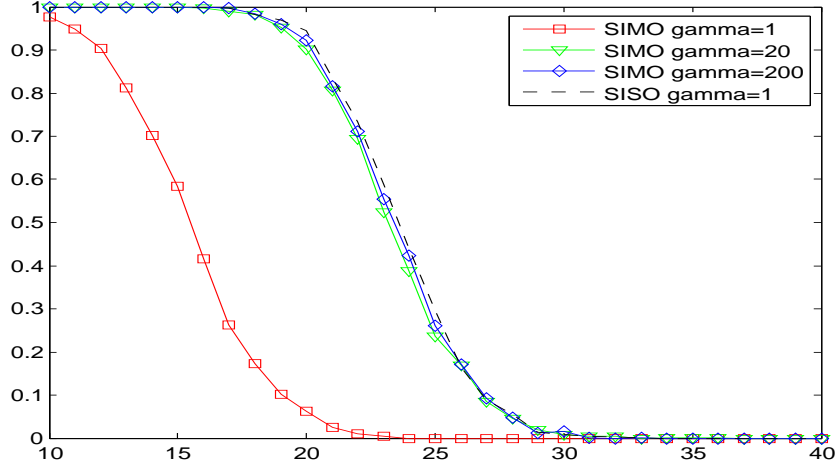


FIGURE 6. Solid curves are the success probabilities for the SIMO measurement at  $\gamma = 1, 20, 200$  and the dashed curve is the SISO Scheme II at  $\gamma = 1$ .

For Scheme III we use equally spaced incident angles  $\theta_l \in [\pi/6, \pi/3]$ , (17) and

$$(33) \quad \theta_l + \tilde{\theta}_l = 2\phi_l + \tilde{\eta}\pi, \quad \tilde{\eta} = 1, 1/2, 1/4.$$

As shown in Figure 5, the performance is essentially independent of  $\tilde{\eta}$ .

Finally, we demonstrate numerically the SIMO schemes studied in [13] and compare their performance with that of the SISO schemes. A particular (one-shot) SIMO scheme relevant here would be to use (23) and (25) but for a fixed incident angle, say  $\theta_l = 0, \forall l$  (In this case (26) is almost certainly violated). In [13] it is established that any SIMO scheme with independent sampling



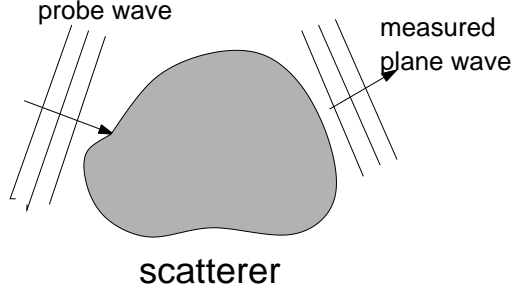


FIGURE 7. Far-field imaging of extended target

angles achieve a nearly optimal performance for a sufficiently high frequency (i.e.  $\gamma \gg 1$ ). The success probabilities of the SIMO scheme for  $\gamma = 1, 20, 200$  are calculated and plotted in Figure 6. Consistent with the theory [13], the low frequency case with  $\gamma = 1$  has the worst performance. Clearly the performance of the one-shot SIMO scheme improves with  $\gamma$  and in the limit  $\gamma \gg 1$  approaches that of the multiple-shot SISO Scheme II. There is negligible difference between the performances for  $\gamma = 20$  and  $\gamma = 200$  both of which follow closely that of the SISO Scheme II with  $\gamma = 1$  (black dashed line in Figure 6).

#### 4. EXTENDED TARGETS

In this section, we analyze the case of extended targets represented by square-integrable functions  $\nu(x, z)$ .

To this end we use the Littlewood-Paley basis

$$(34) \quad \hat{\psi}(\xi, \zeta) = \begin{cases} (2\pi)^{-1}, & \pi \leq |\xi|, |\zeta| \leq 2\pi \\ 0, & \text{otherwise} \end{cases}$$

or

$$(35) \quad \psi(\mathbf{r}) = (\pi^2 x z)^{-1} (\sin(2\pi x) - \sin(\pi x)) \cdot (\sin(2\pi z) - \sin(\pi z)).$$

Then the following set of functions

$$(36) \quad \psi_{\mathbf{p}, \mathbf{q}}(\mathbf{r}) = 2^{-|\mathbf{p}|/2} \psi(2^{-\mathbf{p}} \mathbf{r} - \mathbf{q}), \quad \mathbf{p}, \mathbf{q} \in \mathbb{Z}^2$$

with

$$2^{-\mathbf{p}} \mathbf{r} = (2^{-p_1} x, 2^{-p_2} z)$$

forms an orthonormal wavelet basis in  $L^2(\mathbb{R}^2)$  [11]. In the Littlewood-Paley basis  $\nu$  has the expansion

$$(37) \quad \nu(x, z) = \sum_{\mathbf{p}, \mathbf{q} \in \mathbb{Z}^2} \nu_{\mathbf{p}, \mathbf{q}} \psi_{\mathbf{p}, \mathbf{q}}(x, z).$$

With the incident fields

$$u_k^i(\mathbf{r}) = e^{i\omega \mathbf{r} \cdot \mathbf{d}_k}$$

we have from (4), (6) and (37) that

$$(38) \quad Y_k = 2\pi \sum_{\mathbf{p}, \mathbf{q} \in \mathbb{Z}^2} 2^{|\mathbf{p}|_1/2} \nu_{\mathbf{p}, \mathbf{q}} e^{i\omega 2^{\mathbf{p}}(\mathbf{d}_k - \hat{\mathbf{r}}_k) \cdot \mathbf{q}} \hat{\psi}(\omega 2^{\mathbf{p}}(\hat{\mathbf{r}}_k - \mathbf{d}_k)), \quad k = 1, \dots, n.$$

Define the sensing matrix elements to be

$$(39) \quad A_{k,l} = \frac{1}{2n_{\mathbf{p}} + 1} \hat{\psi}(\omega 2^{\mathbf{p}}(\hat{\mathbf{r}}_k - \mathbf{d}_k)) e^{i\omega 2^{\mathbf{p}}(\mathbf{d}_k - \hat{\mathbf{r}}_k) \cdot \mathbf{q}}$$

and let  $\mathbf{A} = [A_{k,l}]$ , where  $\mathbf{d}_k, \hat{\mathbf{r}}_k$  are given below.

Let

$$\begin{aligned} l &= \sum_{j_1=-p_*}^{p_1-1} \sum_{j_2=-p_*}^{p_2-1} (2m_{\mathbf{j}} + 1)^2 + (q_1 + m_{\mathbf{p}})(2m_{\mathbf{p}} + 1) + (q_2 + m_{\mathbf{p}} + 1), \quad |\mathbf{q}|_{\infty} \leq m_{\mathbf{p}}, \quad |\mathbf{p}|_{\infty} \leq p_*, \\ k &= \sum_{j_1=-p_*}^{p'_1-1} \sum_{j_2=-p_*}^{p'_2-1} (2m_{\mathbf{j}} + 1)^2 + (q'_1 + m_{\mathbf{p}'}) (2m_{\mathbf{p}'} + 1) + (q'_2 + m_{\mathbf{p}'} + 1), \quad |\mathbf{q}'|_{\infty} \leq n_{\mathbf{p}'}, \quad |\mathbf{p}'|_{\infty} \leq p_*, \end{aligned}$$

for some  $m_{\mathbf{p}}, n_{\mathbf{p}}, p_* \in \mathbb{N}$ , be the column and row indexes, respectively, of  $\mathbf{A}$ . Note how  $k$  is related to  $\mathbf{p}'$  in the above expression which is important to understand the scheme described below.

Let  $\xi_k, \zeta_k$  be independent, uniform random variables on  $[-1, 1]$  and define

$$(40) \quad \alpha_k = \frac{\pi}{\omega_k 2^{p'_1}} \cdot \begin{cases} 1 + \xi_k, & \xi_k \in [0, 1] \\ -1 + \xi_k, & \xi_k \in [-1, 0] \end{cases}$$

$$(41) \quad \beta_k = \frac{\pi}{\omega_k 2^{p'_2}} \cdot \begin{cases} 1 + \zeta_k, & \zeta_k \in [0, 1] \\ -1 + \zeta_k, & \zeta_k \in [-1, 0] \end{cases}.$$

Suppose  $\alpha_k, \beta_k \in [-1, 1]$  for all  $\mathbf{p}', |\mathbf{p}'| \leq p_*$ . This holds true, for example, when the frequencies  $\omega_k$  satisfy the constraint

$$(42) \quad \omega_k 2^{p'_1} \geq 2\pi, \quad \omega_k 2^{p'_2} \geq 2\pi.$$

Let  $(\rho_k, \phi_k)$  be the polar coordinates of  $(\alpha_k, \beta_k)$ .

As before, let  $\theta_k, \tilde{\theta}_k$  be the angles of incidence and sampling, respectively, which are chosen according to

$$(43) \quad -2 \sin \frac{\theta_k - \tilde{\theta}_k}{2} \sin \frac{\theta_k + \tilde{\theta}_k}{2} = \alpha_k = \rho_k \cos \phi_k$$

$$(44) \quad 2 \sin \frac{\theta_k - \tilde{\theta}_k}{2} \cos \frac{\theta_k + \tilde{\theta}_k}{2} = \beta_k = \rho_k \sin \phi_k.$$

in analogy to (14)-(15). This means

$$(45) \quad -\omega_k 2^{\mathbf{p}}(\hat{\mathbf{r}}_k - \mathbf{d}_k) = \omega_k(2^{p_1} \alpha_k, 2^{p_2} \beta_k) = \pi(2^{p_1-p'_1}(\pm 1 + \xi_k), 2^{p_2-p'_2}(\pm 1 + \zeta_k))$$

where the signs are given by the signs of  $\xi_k, \zeta_k$ , respectively.

By (45) and the definition of  $\hat{\psi}$  it is clear that  $A_{k,l}$  are zero if  $\mathbf{p} \neq \mathbf{p}'$ . Consequently the sensing matrix is the block-diagonal matrix with each block (indexed by  $\mathbf{p} = \mathbf{p}'$ ) in the form of random Fourier matrix

$$(46) \quad A_{k,l} = \frac{1}{2n_{\mathbf{p}} + 1} e^{i\pi(q_1 \xi_k + q_2 \zeta_k)}.$$

Let  $X = (X_l)$  with

$$X_l = 2\pi(2n_{\mathbf{p}} + 1)2^{|\mathbf{p}|_1/2}\nu_{\mathbf{p},\mathbf{q}}$$

be the target vector. Let

$$m = \sum_{j_1=-p_*}^{p_*} \sum_{j_2=-p_*}^{p_*} (2m_{\mathbf{j}} + 1)^2.$$

We can then write the measurement vector  $Y = \mathbf{A}X$  where  $\mathbf{A} \in \mathbb{C}^{n \times m}$ . The above observation means that the target structures of different dyadic scales are decoupled and can be determined separately by our approach using compressed sensing techniques.

To solve (43)-(44) we consider

$$(47) \quad \theta_k + \tilde{\theta}_k = 2\phi_k + \pi$$

and

$$(48) \quad 2 \sin \frac{\theta_k - \tilde{\theta}_k}{2} = \rho_k.$$

The simplest way to satisfy the relationships (47) and (48) is to set

$$(49) \quad \theta_k = \phi_k + \frac{\pi}{2} + \arcsin \frac{\rho_k}{2}$$

$$(50) \quad \tilde{\theta}_k = \phi_k + \frac{\pi}{2} - \arcsin \frac{\rho_k}{2}$$

analogous to (24) and (25).

In the case of extreme anisotropy (needle-like structure), say  $2^{p_1-p_2} \gg 1$

$$\phi_k \approx \pm \frac{\pi}{2}$$

and hence

$$(51) \quad \theta_k + \tilde{\theta}_k \approx 0.$$

On the other hand if  $2^{p_1-p_2} \ll 1$  then

$$\phi_k \approx \pm \pi$$

and hence

$$(52) \quad \theta_k + \tilde{\theta}_k \approx \pi.$$

Relations (51) and (52) are reminiscent of Snell's law of reflection if  $\tilde{\theta}_k$  are interpreted as the reflection angles.

Using the RIP for the random Fourier matrix of each block, we obtain the following theorems analogous to Theorems 1 and 2.

**Theorem 3.** For each  $\mathbf{p}$ ,  $|\mathbf{p}| \leq p_*$ , let (13) be satisfied for  $n = n_{\mathbf{p}}$  and  $\sigma = 2s_{\mathbf{p}}$  and any  $\delta < \sqrt{2} - 1$ .

Let  $\xi_l, \zeta_l$  be independently and uniformly distributed in  $[-1, 1]$ . Let the incident and sampling angles be determined by (40)-(41), (43)-(44).

Then (9) is satisfied for the  $\mathbf{p}$ -block of the sensing matrix with probability at least  $1 - \alpha$ . Consequently the solution  $\hat{X}_{\mathbf{p}}$  by BP (8) satisfies

$$(53) \quad \|\hat{X}_{\mathbf{p}} - X_{\mathbf{p}}\|_1 \leq C_0 \|X_{\mathbf{p}} - X_{\mathbf{p}}^{(s_{\mathbf{p}})}\|_1$$

$$(54) \quad \|\hat{X}_{\mathbf{p}} - X_{\mathbf{p}}\|_2 \leq C_0 s_{\mathbf{p}}^{-1/2} \|X_{\mathbf{p}} - X_{\mathbf{p}}^{(s_{\mathbf{p}})}\|_1$$

for some constant  $C_0$ .

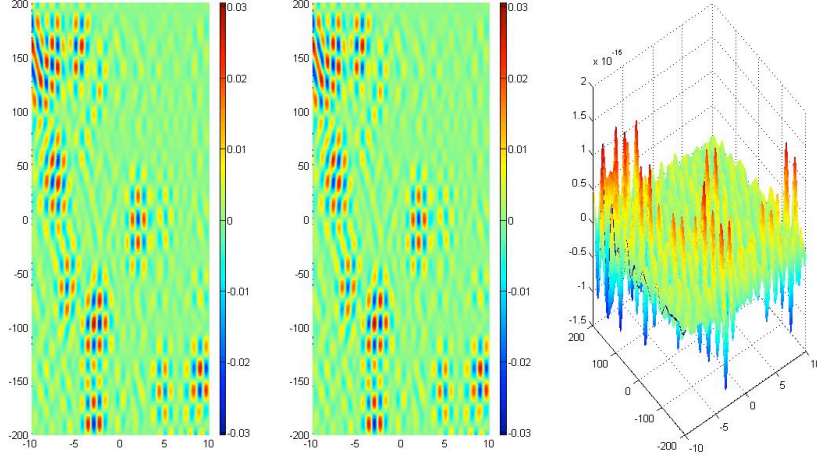


FIGURE 8. Imaging of an extended target of the scales  $(32, 1)$ : The left plot is a part of the exact structure; the middle plot is the corresponding part of the reconstructed profile; the right plot shows the (round-off) error.

**Theorem 4.** *Let  $Y_{\mathbf{p}}$  be contaminated by noise of size  $\varepsilon$  and let  $\hat{X}_{\mathbf{p}}$  be the corresponding solution to (29). Under the assumptions of Theorem 3, we have*

$$(55) \quad \|\hat{X}_{\mathbf{p}} - X_{\mathbf{p}}\|_2 \leq C_0 s_{\mathbf{p}}^{-1/2} \|X_{\mathbf{p}} - X_{\mathbf{p}}^{(s_{\mathbf{p}})}\|_1 + C_1 \varepsilon$$

with probability at least  $1 - \alpha$  where  $C_0$  and  $C_1$  are constants.

The numerical results with  $\mathbf{p} = (5, 0)$ ,  $m_{\mathbf{p}} = 10$ ,  $s_{\mathbf{p}} = 42$  are shown in Figure 8.

## 5. CONCLUSION AND DISCUSSION

We have proposed, analyzed and numerically tested several SISO sampling schemes which transform the scattering matrix into the random Fourier matrix in the case of point scatterers and the block-diagonal form of random Fourier matrices in the case of extended targets.

In the case of point scatterers, these sampling schemes are either multi-frequency band limited (I) or single frequency outside band (II). For Scheme I, the sampling direction is the backward direction analogous to synthetic aperture radar (SAR) while for Scheme II in the high frequency limit the optimal sampling direction is in the forward direction, analogous to the X-ray tomography. Both schemes produce nearly the same recovery probability with the resolution given by (27), i.e.

$$\ell = \frac{\pi}{\sqrt{2\Omega}}.$$

In the case of extended targets, the block-diagonal form of the scattering matrix means that different dyadic scales of the target are decoupled and can be imaged scale-by-scale separately by our method. The condition (42) implies that the wavelengths are no larger than the scales under interrogation. Both results are in line with the classical resolution criterion.

The SIMO schemes in which the scattered field of an incident angle is measured at multiple sampling angles have been studied in [13, 14, 15]. Except for the special case of the periodic

scatterers lying on a transverse plane [14], it is not known if the sensing matrices of the SIMO schemes in general satisfy the RIP or not. In this case, the approach based on the notion of incoherence is taken to analyze the SIMO schemes [13, 15]. This approach is generally more flexible and should be applicable to the SISO schemes considered here.

The main advantage of the SIMO schemes is that in the one-shot setting (one incident field) the inverse scattering problem can be solved exactly *without* the Born approximation by inverting an auxiliary nonlinear system of equations [13]. We are working to extend the idea to the multiple-shot setting for both the SIMO and SISO schemes.

On the other hand, the SISO schemes with the RIP tend to have a better performance which can be matched by that of the SIMO schemes only at high frequency as demonstrated in Figure 6. The high frequency behavior of the SIMO schemes is analyzed in detail in [13].

**Acknowledgement.** I thank my students Hsiao-Chieh Tseng (Figures 1-6) and Wenjing Liao (Figure 7) for preparing the figures.

## REFERENCES

- [1] M. Born and E. Wolf, *Principles of Optics*, 7-th edition, Cambridge University Press, 1999.
- [2] A.M. Bruckstein, D.L. Donoho and M. Elad, "From sparse solutions of systems of equations to sparse modeling of signals," *SIAM Rev.* **51** (2009), 34-81.
- [3] E. J. Candès, "The restricted isometry property and its implications for compressed sensing," *Compte Rendus de l'Academie des Sciences, Paris, Serie I.* **346** (2008) 589-592.
- [4] E. J. Candès, J. Romberg and T. Tao, "Robust uncertainty principles: Exact signal reconstruction from highly incomplete frequency information," *IEEE Trans. Inform. Theory* **52** (2006), 489-509.
- [5] E.J. Candès, J. Romberg and T. Tao, "Stable signal recovery from incomplete and inaccurate measurements," *Commun. Pure Appl. Math.* **59** (2006), 1207-1234.
- [6] E. J. Candès and T. Tao, "Decoding by linear programming," *IEEE Trans. Inform. Theory* **51** (2005), 4203-4215.
- [7] E. J. Candès and T. Tao, "Near-optimal signal recovery from random projections: universal encoding strategies?," *IEEE Trans. Inform. Theory* **52** (2006), 54-6-5425.
- [8] S.S. Chen, D.L. Donoho and M.A. Saunders, "Atomic decomposition by basis pursuit," *SIAM Rev.* **43** (2001), 129-159.
- [9] D. Colton and R. Kress, *Inverse Acoustic and Electromagnetic Scattering Theory*. 2nd edition, Springer, 1998.
- [10] W. Dai and O. Milenkovic, "Subspace pursuit for compressive sensing: closing the gap between performance and complexity," arXiv:0803.0811.
- [11] I. Daubechies, *Ten Lectures on Wavelets*. SIAM, Philadelphia, 1992.
- [12] D.L. Donoho and X. Huo, "Uncertainty principle and ideal atomic decomposition," *IEEE Trans. Inform. Theory* **47** (2001), 2845-2862.
- [13] A. Fannjiang, "Compressive inverse scattering I. High frequency SIMO measurements," arXiv: 0906.5405
- [14] A. Fannjiang, "Compressive imaging of subwavelength structures," arXiv:0905.3015.
- [15] A. Fannjiang, P. Yan and Thomas Strohmer, "Compressed remote sensing of sparse objects," arXiv:0904.3994
- [16] H. Rauhut, "Stability results for random sampling of sparse trigonometric polynomials," preprint, 2008.
- [17] M. Rudelson and R. Vershynin, "On sparse reconstruction from Fourier and Gaussian measurements," *Comm. Pure Appl. Math.* **111** (2008) 1025-1045.

E-mail address: fannjiang@math.ucdavis.edu

DEPARTMENT OF MATHEMATICS, UNIVERSITY OF CALIFORNIA, DAVIS, CA 95616-8633